



Numerical simulation of molecular uptake via electroporation

Jianbo Li, Hao Lin*

Mechanical and Aerospace Engineering, Rutgers, The State University of New Jersey, 98 Brett Road, Piscataway, NJ 08854, USA

ARTICLE INFO

Article history:

Received 4 June 2010

Received in revised form 14 April 2011

Accepted 19 April 2011

Available online 28 April 2011

Keywords:

Electroporation

Electrophoresis

Molecular delivery

Field-amplified sample stacking

ABSTRACT

A numerical study of electroporation-mediated molecular delivery is presented. The model consists of the Nernst–Planck equations for species transport, coupled with an asymptotic Smoluchowski equation for membrane permeabilization. The transfer of calcium ions into a Chinese Hamster Ovary cell is simulated. The results reveal important physical insights. First, for this particular case, ion electrophoresis plays an important role, and is an order of magnitude faster than free diffusion on a comparable time scale. Second, the maximum achievable concentration within the cell is reciprocally correlated with the extracellular electrical conductivity. This behavior is mediated by an electrokinetic mechanism known as field-amplified sample stacking. Through this mechanism, the intracellular ion concentration can reach a level higher than the extracellular one provided that the intra-to-extracellular conductivity ratio is greater than unity. The results corroborate well with data in the literature, and offer a mechanistic interpretation to previous experimental observations. This work is a step toward the quantification of molecular delivery via electroporation.

© 2011 Elsevier B.V. All rights reserved.

1. Introduction

Electroporation is a widely applied technique in both biological research and clinical applications, in areas including cell transfection, protein insertion, gene and drug delivery, cancer therapy, and stem-cell research, among others [1–11]. The process is complex and involves two major aspects. The first is the permeabilization of the membrane via an applied electric field, to provide access to the cytoplasm [12–14]. The second is the transport of biologically active or other molecules into the permeabilized cell, which is a process known as molecular uptake. When successful, the delivered agents stay in the cell to perform functional tasks, and the cell remains viable, and eventually recovers from the induced damage.

Research in the past three decades has led to significant advances in the understanding of the first aspect, namely, membrane permeabilization. As revealed by experimental observations, the transmembrane potential (TMP, see Table 1 for the definition of acronyms) of a cell rises in response to an applied electric pulse [15–20]. When the TMP exceeds a critical threshold, aqueous, conducting pores form on the membrane [21–29], which significantly increases the membrane conductance and allows molecular passage. In the modeling literature, this process is captured by the Smoluchowski equation (SE) [30–33], which statistically describes the evolution of the pore population as a function of the driving TMP. Based on this equation, various groups developed their respective models to predict membrane permeabilization. In particular, Krassowska and co-authors derived an asymptotic version of the Smoluchowski

equation (ASE, [34,35]), which was subsequently used in a series of whole-cell-level simulations [36–38]. Weaver and co-authors implemented the ASE in a transport lattice framework [39] to study a variety of problems including conventional and supra-electroporation, electroporation of single and multiple cells, organelles, and tissue, and irreversible electroporation for cancer treatment [40–45]. Alternatively, Joshi and co-authors solved the SE directly to track the evolution of pore size and population distribution [46–49]. These works collectively provide fundamental understanding of the phenomenon, and quantitative prediction tools to correlate with experimental data, and to help improve the technique.

An extensive body of work also exists to tackle the second aspect, molecular transport. Experimental work helped identify many of the key elements, but the development of a conclusive understanding is still in progress. In general, the behavior of large molecules (such as DNA) is different from that of small, low-weight molecules (such as propidium iodide (PI)) [50]. For DNA, the successful delivery requires the continuous presence of an electric field [51,52], suggesting the importance of electrophoretic forces in the process [53–56]. However, DNA electrophoresis alone is not sufficient for uptake, and additional mechanisms such as DNA aggregation, DNA–membrane interaction, and intracellular diffusion may also have critical involvements [57,58]. The transport of small molecules [59] (with molecular weights less than 4 kDa, [57]), on the other hand, is presumably less complex. Both electrophoresis and free diffusion are believed to contribute, and the process can be described with the Nernst–Planck (NP) model for electrodiffusion [60]. However, different findings exist on the relative importance of the two mechanisms with respect to each other. Specifically, measurements by Pucihar et al. [60] revealed that free diffusion of PI post-pulsation contributed to most of the fluorescence signal collected, whereas a series

* Corresponding author. Tel.: +1 732 445 2322; fax: +1 732 445 3124.

E-mail addresses: jianboli@eden.rutgers.edu (J. Li), hlin@jove.rutgers.edu (H. Lin).

Table 1
Definition of acronyms.

Abbreviation	Definition
TMP	Transmembrane potential
SE	Smoluchowski equation
ASE	Asymptotic Smoluchowski equation
PI	Propidium iodide
NP	Nernst–Planck equation
FASS	Field amplified sample stacking
PAD	Pore area density

of transdermal drug delivery experiments suggested that electrophoresis of charged molecules had a major contribution [61–65].

In this work, we focus on studying the transport of small molecules into an electroporated cell. We aim to establish a model framework to predict the delivery of such molecules, including free ions (e.g., Na^+ , K^+ , Ca^{2+} , and Cl^-), drug molecules (mostly below a few kDa in the transdermal drug delivery studies [66]), and common molecular dyes used for optical measurements (e.g., PI and Fluo-3). In contrast to the previous compartment or simplified diffusion models [60,67–72], we simulate the spatial and temporal evolution of molecular concentrations using the NP equations, where we also include chemical production terms to capture reactive kinetics. For membrane permeabilization, we adopt the ASE [34,35,38], which provides critical information to compute species fluxes across the membrane. As a specific example, we simulate the delivery of calcium ions into a Chinese Hamster Ovary cell. Our results demonstrate good agreement with the fluorescence measurement performed by Gabriel and Teissié [73]. In addition, an analysis of the detailed transport dynamics reveals two important observations. First, for the particular case studied, electrophoresis is the dominant mode for molecular delivery. Second, the intracellular concentration of free calcium ions can be higher than the basal concentration in the extracellular solution, which behavior is mediated by an electrokinetic mechanism known as field-amplified sample stacking (FASS) [74,75]. According to this mechanism, the maximum achievable ion concentration within the cell is reciprocally correlated with the extracellular conductivity. This prediction corroborates well with previous data [76,77]. The observations suggest that the transport of small ions is much more complex than passive diffusion. This work is an important step towards the quantification of molecular delivery via electroporation.

2. Model formulation

2.1. The electrical problem

A schematic of the problem is shown in Fig. 1. The cell is idealized to be a thin, rigid, and spherical shell of radius a . A spherical coordinate system is adopted. The x -axis is chosen to align with the direction of the applied electric field. σ and Φ denote the electrical conductivity and electric potential, and the subscripts i and e denote intra- and extra-cellular, respectively. Because the charge relaxation time (on the order of nano-seconds) is small when compared with the typical time scales we study (micro- to milli-seconds), we adopt the Ohmic equation for the intra- and extra-cellular electric potentials:

$$\nabla \cdot \mathbf{j} = \nabla \cdot (\sigma_{i,e} \nabla \Phi_{i,e}) = 0, \quad (1)$$

where \mathbf{j} is the Ohmic current density vector. This equation is solved for both the intra- and extra-cellular spaces, and the solutions are coupled on the membrane through electric current continuity,

$$\mathbf{n} \cdot (\sigma_{i,e} \nabla \Phi_{i,e}) = C_m \frac{\partial V_m}{\partial t} + g_l (V_m + V_{\text{rest}}) + j_p, \quad (2)$$

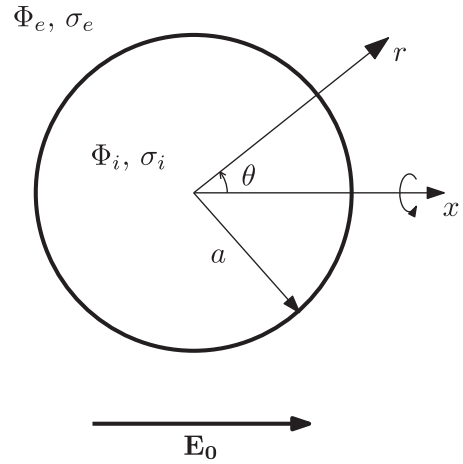


Fig. 1. Schematic of the problem. The x -axis is aligned with the direction of the electric field. r denotes the radial position, and θ is the inclination angle. The problem is axisymmetric with respect to the x -axis.

where \mathbf{n} is the local unit normal vector on the membrane, C_m is the membrane capacitance, g_l is the leakage conductivity, and V_m (defined as $(\Phi_e - \Phi_i)_{r=a}$) and V_{rest} are the transmembrane and the rest potential, respectively. The last term in Eq. (2), j_p , is the total ionic current density through the pores at a specific location on the membrane. Following the treatment by Krassowska and Filev [38], it is calculated using the following formula,

$$j_p(t, \theta) = \sum_{j=1}^{K(t, \theta)} i_p(r_j(t, \theta), V_m) / \Delta A, \quad (3)$$

where ΔA is a local area element, i_p is the current through an individual pore with radius r_j , and K is the total number of pores on the element. Following our previous work [78], i_p is given by

$$i_p = \frac{2\pi r_j^2 \sigma_{\text{eff}} V_m}{\pi r_j + 2h}, \quad (4)$$

where $\sigma_{\text{eff}} = (\sigma_e - \sigma_i) / \ln(\sigma_e / \sigma_i)$ is an effective pore conductivity, and h is the membrane thickness.

2.2. Pore nucleation and evolution

The ASE model to describe the evolution of the pore statistics follows closely that by Krassowska and Filev [38],

$$\frac{dN}{dt} = \alpha e^{(V_m / V_{ep})^2} \left(1 - \frac{N}{N_0 e^{q(V_m / V_{ep})^2}} \right), \quad (5)$$

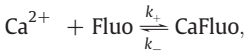
$$\frac{dr_j}{dt} = U(r_j, V_m, \tau), \quad j = 1, 2, \dots, k. \quad (6)$$

Here $N(t, \theta)$ is the local pore number density, α , N_0 , q , and V_{ep} are constants, U is the advection velocity, and τ is an effective membrane tension. According to this model, pores nucleate at an initial radius, $r_* = 0.51$ nm, and at a rate described by Eq. (5). They then evolve in size according to Eq. (6), to minimize the total energy of the lipid membrane. Resealing effects are also captured by the ASE. Further details of the model, as well as relevant parameters, are found in [38], and are not presented here for brevity. Note here we have adopted one particular model among many permeabilization models present in the modern literature [38,39,46,79]. However, the detailed permeabilization process

has no significant effect on molecular delivery as we demonstrate in Section 4.1 below.

2.3. Species transport

We adopt a generalized NP system to simulate species transport. In the following, we consider three specific species, Ca^{2+} , Fluo-3, and the compound CaFluo. These species are involved in typical Ca^{2+} entry experiments [73,80–82]. We assume that the cell is preloaded with Fluo-3 at a molar concentration of $[\text{Fluo}]_{i,o}$, where the subscript i again denotes intracellular, and o denotes an initial value. The initial intra- and extra-cellular Ca^{2+} concentrations are $[\text{Ca}^{2+}]_{i,o}$ and $[\text{Ca}^{2+}]_{e,o}$, respectively (Table 2). When the free calcium ions enter the cell through the permeabilized membrane, they bind to Fluo-3 to form the compound CaFluo, which emits fluorescent signal upon excitation. The reaction is described by



where k_+ and k_- are the association and dissociation rate constants, respectively, and we use “Fluo” to denote Fluo-3. The NP equations are modified with production terms to capture this process:

$$\frac{\partial [\text{Ca}^{2+}]}{\partial t} = \nabla \cdot (w_{\text{Ca}^{2+}} F z_{\text{Ca}^{2+}} [\text{Ca}^{2+}] \nabla \Phi) + \nabla \cdot (D_{\text{Ca}^{2+}} \nabla [\text{Ca}^{2+}]) - k_+ [\text{Fluo}] [\text{Ca}^{2+}] + k_- [\text{CaFluo}], \quad (7)$$

$$\frac{\partial [\text{Fluo}]}{\partial t} = \nabla \cdot (w_{\text{Fluo}} F z_{\text{Fluo}} [\text{Fluo}] \nabla \Phi) + \nabla \cdot (D_{\text{Fluo}} \nabla [\text{Fluo}]) - k_+ [\text{Fluo}] [\text{Ca}^{2+}] + k_- [\text{CaFluo}], \quad (8)$$

$$\frac{\partial [\text{CaFluo}]}{\partial t} = \nabla \cdot (w_{\text{CaFluo}} F z_{\text{CaFluo}} [\text{CaFluo}] \nabla \Phi) + \nabla \cdot (D_{\text{CaFluo}} \nabla [\text{CaFluo}]) + k_+ [\text{Fluo}] [\text{Ca}^{2+}] - k_- [\text{CaFluo}]. \quad (9)$$

Here $[X]$ denotes the molar concentration of the corresponding species X (Ca^{2+} , Fluo, or CaFluo), F is the Faraday constant, z_X is the valence number, D_X is the diffusion coefficient, and w_X is the mechanical mobility (calculated from D_X using Einstein's relation, $D = wRT$, where R is the universal gas constant, and T is temperature). Eqs. (7–9) are solved for both the intra- and extra-cellular spaces, and are coupled on the membrane by continuity of molar flux density for every species:

$$F_{i,e} = F_m, \quad (10)$$

where,

$$F_{i,e} \equiv -\mathbf{n} \cdot (w_X F z_X [X] \nabla \Phi + D_X \nabla [X])_{i,e}, \quad (11)$$

$$F_m \equiv \rho_p \frac{D_X (Pe_X - \ln \gamma) (\gamma - 1) ([X]_e - [X]_i \exp(Pe_X))}{h \ln \gamma (\gamma - \exp(Pe_X))}. \quad (12)$$

Here $F_{i,e}$ are the flux densities from the intra- and extra-cellular spaces, respectively, F_m is the flux density across the membrane, $Pe_X \equiv -w_X F z_X V_m / D_X$ is an effective Péclet number for each species, and $\gamma = \sigma_e / \sigma_i$ the extra-to-intra-cellular conductivity ratio. Eq. (12) is derived assuming that the sum of the electrophoretic and diffusive fluxes is constant along the axis within the pore, and a detailed derivation is found in Appendix A. Note that the Péclet number characterizes the relative importance of electrophoretic to diffusive transport. Equivalently, it can be rewritten as $Pe_X = -F z_X V_m / RT$ using

Einstein's relation, which characterizes the relative importance of electrical to thermal energy. Eqs. (7–12) are coupled to (1–6) through two variables, Φ and ρ_p . The latter is calculated for every area element after the pore statistics is obtained,

$$\rho_p(t, \theta) = \sum_{j=1}^{K(t, \theta)} \pi r_j^2 / \Delta A.$$

Here we name this quantity the “pore area density” (PAD). Evidently, it is the local fractional “opening” area occupied by the pores, and is a measure of membrane permeabilization.

We remark that by adopting the NP framework, i.e., Eqs. (7–12), we have ignored the effects of electro-osmotic flow on species transport. A discussion is found in Appendix B, where its importance and impact are estimated.

2.4. Numerical implementation

Eqs. (1–10) are solved numerically using a finite volume, alternative direction implicit (ADI) scheme. The problem is effectively two-dimensional as we assume axisymmetry about the x -axis. For initial conditions, we assume

$$N(0, \theta) = 0, \quad \Phi_i(0, r, \theta) = V_{\text{rest}}, \quad \Phi_e(0, r, \theta) = 0.$$

The initial concentrations for Ca^{2+} and intracellular Fluo-3 ($[\text{Ca}^{2+}]_{i,o}$, $[\text{Ca}^{2+}]_{e,o}$, and $[\text{Fluo}]_{i,o}$) are given in Table 2. The initial concentrations for extracellular Fluo-3, and CaFluo everywhere are zero. The simulation domain is a large sphere $20a$ in radius. On the outer boundary, we prescribe

$$\Phi_e(t, r = 20a, \theta) = -E_0 r \cos \theta,$$

where E_0 is the strength of the applied field. This prescription well-approximates the ambient condition of a uniform electric field. To implement Eq. (10), the flux density across the membrane, F_m , is first

Table 2
List of model parameters.

Symbol	Definition	Value
a	Cell radius	8 μm [73]
h	Membrane thickness	5 nm
σ_i	Intracellular conductivity	0.5 S/m [89]
σ_e	Extracellular conductivity	0.15 S/m [73]
F	Faraday constant	96485 C/mol
R	Universal gas constant	8.314 J/K·mol
T	Room temperature	298.15 K
k_+	Association rate constant	80 (μM) $^{-1}$ [84]
k_-	Dissociation rate constant	90 s $^{-1}$ [84]
$D_{\text{Ca}^{2+},i}$	Diffusion coefficient of Ca^{2+} in the cytoplasm	250 $\mu\text{m}^2/\text{s}$ [84]
$D_{\text{Ca}^{2+},e}$	Diffusion coefficient of Ca^{2+} in the extracellular solution	790 $\mu\text{m}^2/\text{s}$ [85]
$D_{\text{Fluo},i}$	Diffusion coefficient of Fluo-3 in the cytoplasm	20 $\mu\text{m}^2/\text{s}$ [84]
$D_{\text{Fluo},e}$	Diffusion coefficient of Fluo-3 in the extracellular solution	90 $\mu\text{m}^2/\text{s}$ [84]
$D_{\text{CaFluo},i}$	Diffusion coefficient of CaFluo in the cytoplasm	20 $\mu\text{m}^2/\text{s}$ [84]
$D_{\text{CaFluo},e}$	Diffusion coefficient of CaFluo in the extracellular solution	90 $\mu\text{m}^2/\text{s}$ [84]
$z_{\text{Ca}^{2+}}$	Valence number of Ca^{2+}	+2
z_{Fluo}	Valence number of Fluo-3	−5 [84]
z_{CaFluo}	Valence number of CaFluo	−3
$[\text{Ca}^{2+}]_{i,o}$	Initial Ca^{2+} concentration in the cytoplasm	220 nM [73]
$[\text{Ca}^{2+}]_{e,o}$	Initial Ca^{2+} concentration in the extracellular solution	1 mM [73]
$[\text{Fluo}]_{i,o}$	Initial Fluo-3 concentration in the cytoplasm	2.2 μM [73]
E_0	Applied electric field strength	1.0 kV/cm [73]

computed given $[X]_e$, $[X]_i$, ρ_p , V_m , etc. The resulting value is then used to prescribe the boundary flux densities, F_i and F_e , for the intra- and extra-cellular spaces, respectively. A non-uniform spherical grid with higher resolution around the membrane is adopted to optimize computational efficiency. The numerical convergence is tested with respect to resolution by increasing the number of grids. All general parameters pertinent to the permeabilization model (1–6) are taken from [38], and are not repeated here for brevity. Parameters specific to this study (e.g., $\sigma_{i,e}$, a , and E_0), and the rate constants are summarized in Table 2. They are specified to best approximate the experimental conditions in [73]. This problem is the primary focus of the study presented below.

3. Results

In this section, we first present the simulated results of a cell permeabilized with a single, 6-ms-long pulse. The cell radius is $a = 8 \mu\text{m}$, and the field strength is $E_0 = 1 \text{ kV/cm}$. The species transport is examined in detail, and is compared with the fluorescence measurements by Gabriel and Teissie [73] (denoted as GT99 in the following). The effect of FASS, and the specific roles of electrophoresis and diffusion in delivery, are then studied and discussed.

Fig. 2 summarizes the results on the electric potential and membrane permeabilization. Fig. 2a shows the electric potential

contour along the cell center-plane at $t = 20 \mu\text{s}$ (see also Movie 1 in the online supplementary material). Outside the cell, the contours become uniformly distributed a couple of diameters away, indicating convergence of the electric field to the ambient, constant condition. The contours are less populated within the cell, suggesting a lower electric field, which we will further examine below. The presence of a TMP is evident as the contour lines are discontinuous at the membrane. In Fig. 2b, the TMP is shown as a function of θ , the location along the membrane. At $t = 0.5 \mu\text{s}$, the TMP exhibits a cosinusoidal shape, consistent with a non-permeabilized membrane. Further increase in the TMP results in permeabilization around the polar caps ($t = 20 \mu\text{s}$ and 6 ms), and a depression in the profile due to an increased membrane conductivity. Fig. 2c shows the PAD, also as a function of θ . Only the areas around the cathode- and anode-facing poles ($\theta = 0, \pi$) are permeabilized. (Note here the anode is the positive, and the cathode is the negative electrode, as our device consumes power.) The slight asymmetry in the profile is due to the existence of a rest potential, V_{rest} . Fig. 2d shows the development of the PAD for $\theta = 0, \pi$. At $t = 6 \text{ ms}$, the PAD at the polar caps is approximately equal in magnitude (~ 0.008). After the electric field ceases, the PAD drops dramatically to $\sim 10^{-5}$. For both V_m and ρ_p , a rapid rise occurs within the first $20 \mu\text{s}$, followed by a slow and gradual adjustment for the rest of the pulse duration. Other basic trends agree with the predictions by Krassowska and Filev [38], although different

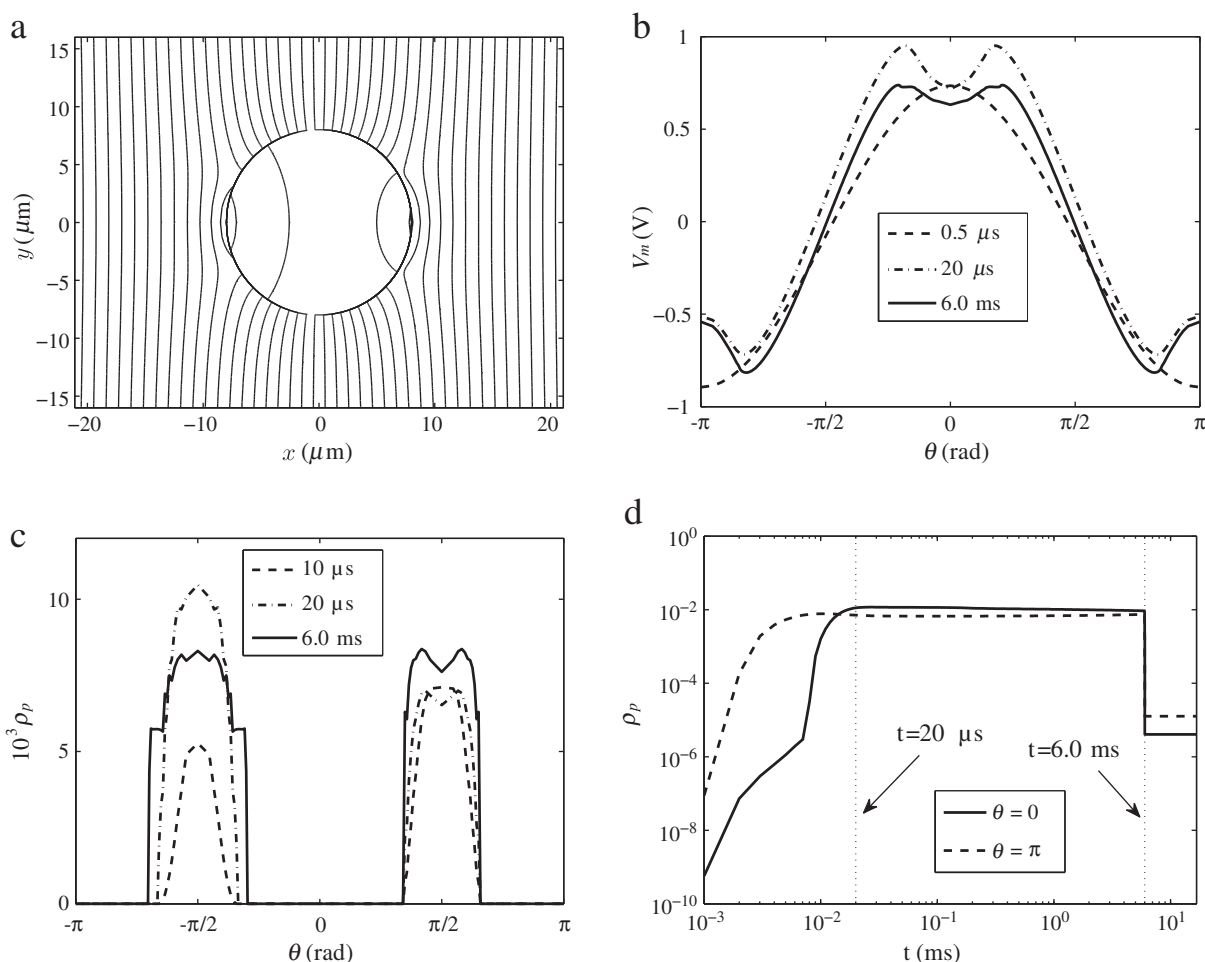


Fig. 2. Simulated cell permeabilization. (a) The electric potential contour at $t = 20 \mu\text{s}$. The direction of the applied field is from left to right. (b) TMP distribution along the membrane at various times. Here θ is the polar angle, and $\theta = 0, \pi$ correspond to the cathode- and anode-facing pole, respectively (see Fig. 1). (c) PAD distribution along the membrane at various times. (d) The time course of PAD at $\theta = 0, \pi$.

cell type, size, and pulsing scheme are used here. In this work, we focus on the study of species transport, and further details on the pore dynamics and permeabilization characteristics are not presented for brevity.

Fig. 3 shows the evolution of molar concentration for the various species involved. The concentrations are shown in color contours, where red denotes high, and blue denotes low values. The specific values are plotted in Fig. 4. For the first three rows ($[Ca^{2+}]$, $[Fluo]$, and $[CaFluo]$), the contour is taken at the center-plane of the cell. The times correspond to those in GT99. The results for $[Ca^{2+}]$ show clearly that the ions enter from the anode-facing (positive) side during the first 6 ms, driven by electrophoretic forces. After the pulse ceases, they slowly diffuse away within the cell, as indicated by the decrease in intensity from 10 to 16.7 ms (see Movie 2 in the online supplementary material). The peak concentration is around 10.5 mM, much higher than the basal extracellular concentration, $[Ca^{2+}]_{e,o} = 1$ mM. The cause for this phenomenon is explained later. Because $[Ca^{2+}]$ is much higher than the initial Fluo-3 concentration, $[Fluo]_{i,o} = 2.2 \mu M$, the product concentration, $[CaFluo]$, is limited by the latter. The contour plot for $[Fluo]$ shows a near-uniform value (see also Fig. 4b), with a receding front due to consumption. The $CaFluo$ concentration is at a similar level (see also Fig. 4c), but with an advancing front complementary to that of $[Fluo]$. Because the reaction is relatively fast (with a characteristic time of μs), the spreading of the $CaFluo$ profile is mainly driven by that of Ca^{2+} , i.e., by electrophoresis for $t < 6$ ms, and by diffusion afterwards.

A comparison of $[CaFluo]$ evolution with the fluorescence measurement by GT99 (Fig. 3, bottom row) shows both agreement and discrepancy. The spreading dynamics in general agree with each other, although the simulation slightly over-predicts the rate of front propagation. The discrepancy lies in that the experimental result shows a gradual increase in the fluorescence intensity, whereas the simulation predicts a near-uniform $CaFluo$ concentration. We argue that the non-uniformity observed in the experiments is mainly from an optical effect. Note that we plot $[CaFluo]$ at the (infinitesimally thin) center-plane from the simulation, whereas the fluorescence measurement results from light emission integrated over a finite optical depth. To reconcile the difference, we define a convolved concentration,

$$[CaFluo]_{conv} \equiv \int_{-\sigma_z/2}^{\sigma_z/2} [CaFluo] e^{-z^2/2\sigma_z^2} dz \quad (13)$$

where $\sigma_z = 18 \mu m$ is the focal depth from an earlier work by the same authors, and the z -direction is perpendicular to the focal plane [83]. The result (Fig. 3, the fourth row) shows a desired characteristic comparable to that in the experiment. An explanation for this behavior is found below.

In Fig. 4, the concentration profiles are plotted along the cell centerline for various times. The cell symmetrically spans from $x = -8$ to $8 \mu m$. As stated above, the Ca^{2+} concentration reaches 10.5 mM soon after entering the cell (at $t = 4 \mu s$, not shown), and propagates

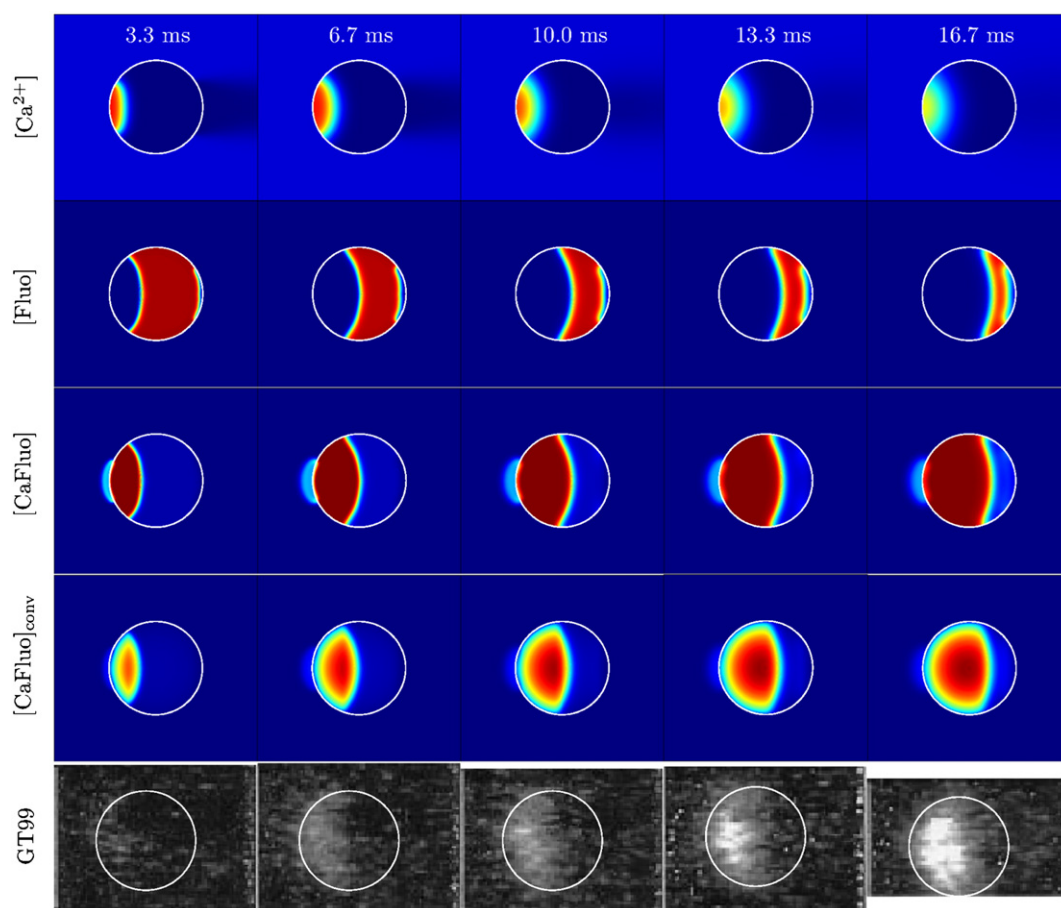


Fig. 3. Evolution of species concentration at the cell center-plane (top 3 rows), at times corresponding to those in GT99 (bottom row, adapted with permission). The fourth row shows a convolved concentration, $[CaFluo]_{conv}$, computed with Eq. (13). For the simulated results, red denotes high, and blue denotes low values. White circles denote the membrane.

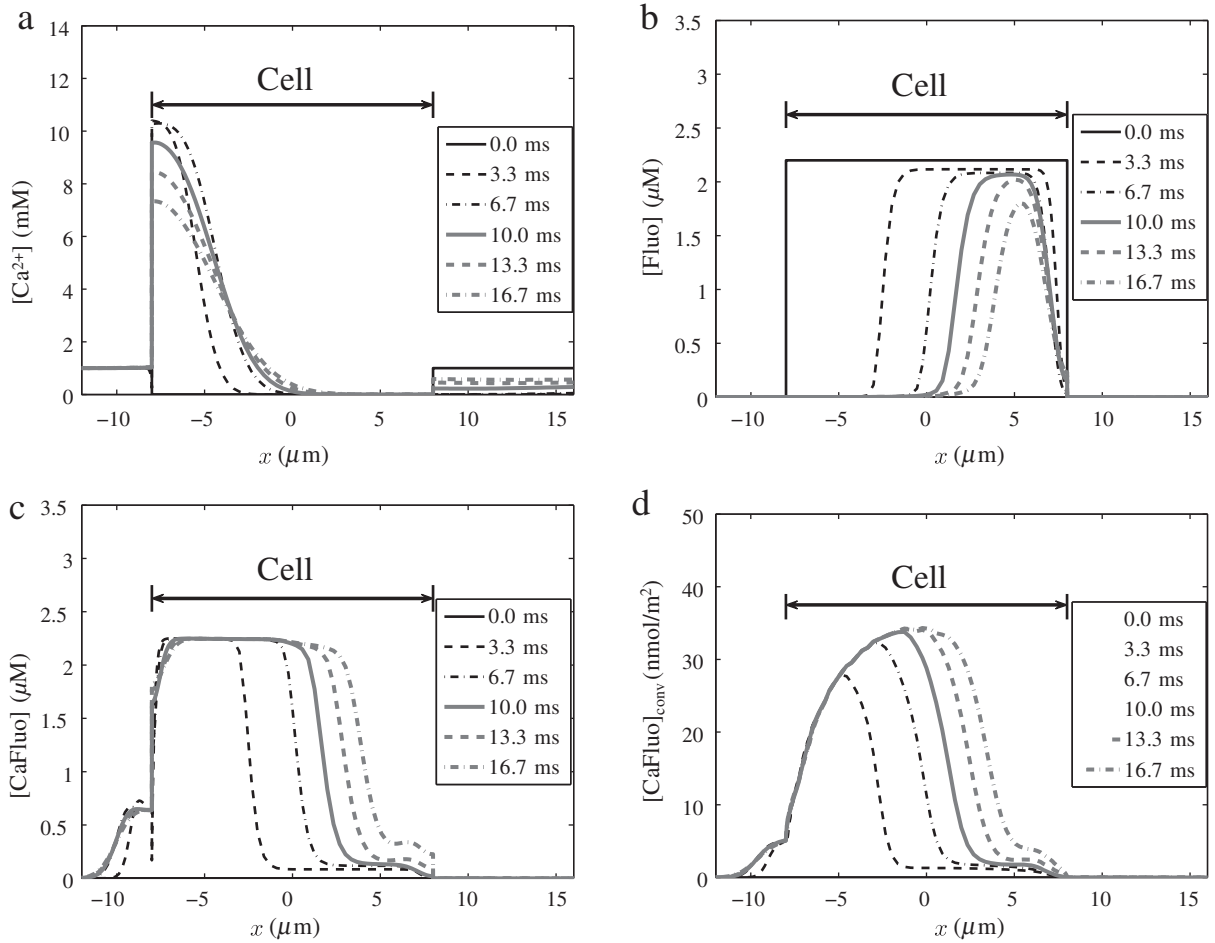


Fig. 4. Species concentrations along the cell centerline. Fig. 4d provides a favorable agreement when compared with Fig. 2b in GT99.

rightward electrophoretically. After the pulse ceases ($t > 6$ ms), the peak decays, and the profile spreads due to free diffusion. It is interesting to note the depletion outside the cathode-facing cap. In Fig. 4b and c, the peak values for both [Fluo] and [CaFluo] are around $2.2 \mu\text{M}$, which are determined by the preloaded Fluo-3 concentration. Note that in Fig. 4c, a slight leakage is found left to the cell. This effect is induced again by electrophoresis, because CaFluo has a valence number of -3 (Table 2). In Fig. 4d, the convolved CaFluo concentration is shown. Peaks in the value appear in the profiles, which gradually increase over time. This effect is explained by the following considerations. 1) The focal depth, $\sigma_z = 18 \mu\text{m}$, is greater than the cell diameter, $2a = 16 \mu\text{m}$. Light emission from the entire cell is thus collected. 2) However, the cell is “thicker” at the center, and “thinner” on the edge. Therefore, a near-uniform [CaFluo] would give rise to a non-uniform [CaFluo]_{conv}, which we assume to correlate with the fluorescence intensity. Fig. 4d provides a favorable comparison with Fig. 2b in GT99, which is not reproduced here. This result suggests that care needs to be taken when attempting to calculate molar concentration values from fluorescence measurements in such situations.

The high intracellular Ca^{2+} concentration observed in Figs. 3 and 4 can be explained by a known mechanism termed “field-amplified sample stacking” (FASS) [74,75]. The concentration elevation is caused by a non-uniform electrophoretic velocity across the membrane. Here we present a simplified, one-dimensional argument. We restrict our considerations to the cell centerline, along which all

vectors are uni-directional due to symmetry. The axial electrophoretic velocity, U_{ep} , is shown in Fig. 5a, and is calculated with the formula $U_{ep} = wFzE_x$, where E_x is the axial electric field. The variation in U_{ep} has contributions from two sources. The first one is in E_x , which is shown in Fig. 5b. At the cell interfaces ($x = \pm 8 \mu\text{m}$), the Ohmic law (Eq. (1)) requires that $\sigma_e E_{x,e} = \sigma_i E_{x,i}$, such that $E_{x,e} = E_{x,i}(\sigma_i/\sigma_e)$. The extracellular field is thus higher due to a lower buffer conductivity (Table 2). Further variations of the field inside and outside of the cell are due to geometric effects. The second is from the fact that calcium ions diffuse approximately three times more slowly within the cell (Table 2) [84,85]. Using Einstein's relation, $w = D/RT$, the mechanical mobility within the cell is also smaller by the same proportion. The combined contributions give rise to an order of magnitude decrease in U_{ep} across the membrane. Qualitatively, when the ions enter from the anode-facing side electrophoretically, they experience a sudden slow-down, and hence “stack” in a manner similar to that of a traffic jam. Quantitatively, the concentration enhancement can be estimated via a simple calculation. By flux continuity, $F_i = F_e$ (Eq. (10)), and temporarily ignoring diffusion, we have

$$(U_{ep}c)_i = (U_{ep}c)_e, \quad \text{at the membrane,} \quad (14)$$

where c is a generic species concentration. If we further assume that c_e remains to be the ambient, initial value (denoted by $c_{e,o}$), and that c_i at

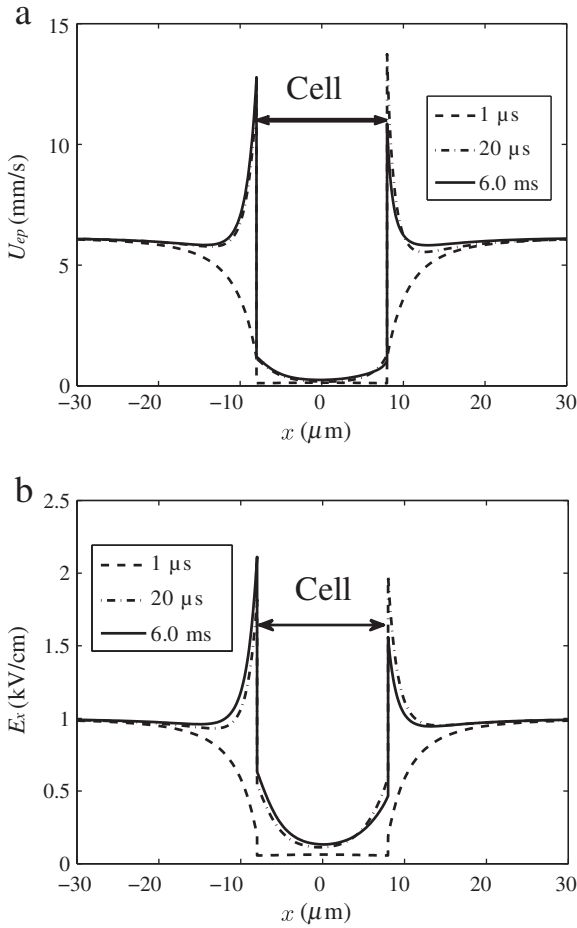


Fig. 5. a) The axial electrophoretic velocity. b) The axial electric field. Both quantities are plotted along the cell centerline.

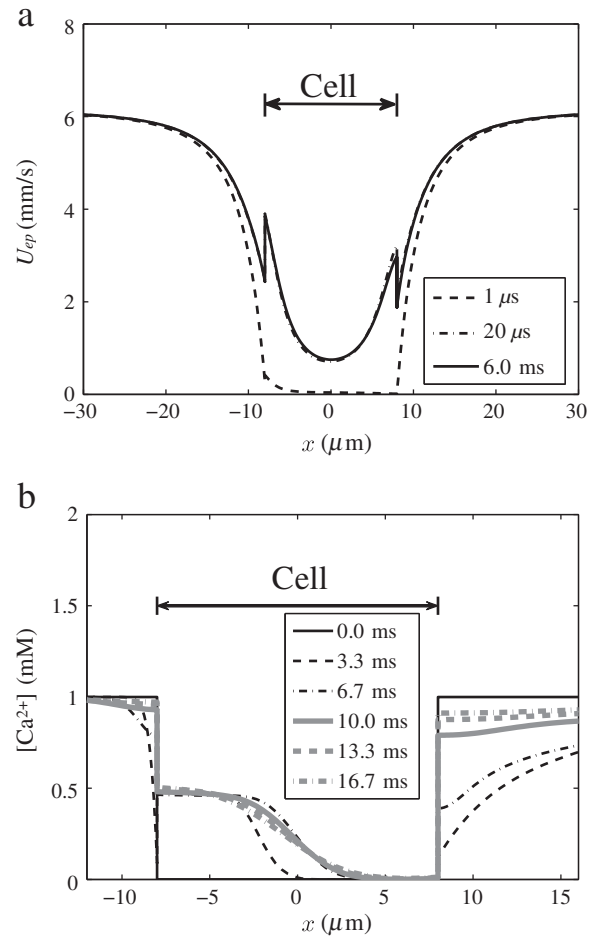


Fig. 6. Concentration rarefaction, for $\sigma_i/\sigma_e = 0.2$. a) The axial electrophoretic velocity. b) Ca^{2+} concentration. Both quantities are plotted along the cell centerline.

the membrane is the maximum achievable concentration (denoted by $c_{i,\max}$), we then have

$$\Gamma = \frac{c_{i,\max}}{c_{e,0}} = \left(\frac{\sigma_i}{\sigma_e}\right) \left(\frac{D_e}{D_i}\right), \quad (15)$$

where D_i and D_e are respectively the intra- and extra-cellular diffusion coefficient, and Γ is the “stacking ratio”. Eq. (15) is derived following a standard FASS theory [74,75]. Although significant simplifications are involved, it does provide a reasonable and convenient estimate. For example, for the present case, Eq. (15) yields $\Gamma = 10.5$, in close agreement with the value from the simulation. Moreover, it clearly indicates that

$$c_{i,\max} \propto 1 / \sigma_e. \quad (16)$$

Further discussions and comparisons with experiments are found in the next section.

Interestingly, Eq. (15) also indicates that $\Gamma < 1$, or rarefaction, can occur. Indeed, when we set $(\sigma_i/\sigma_e) = 0.2$, but keeping all other parameters identical, we observe a concentration decrease within the cell (Fig. 6). For this case, Eq. (15) gives $\Gamma = 0.63$, and the simulation gives $\Gamma = 0.75$. Note that in Fig. 6a, although in general it appears that $U_{ep,e} > U_{ep,i}$, what dictates rarefaction is the velocity difference right across the membrane (at $x = \pm 8 \mu\text{m}$), where $U_{ep,e} < U_{ep,i}$.

Last but not least, the respective effects of electrophoresis and free diffusion on delivery are investigated. In Fig. 7a, the solid curve shows the total moles of Ca^{2+} (denoted by $[\text{Ca}^{2+}]_{\text{tot}}$) within the cell as a function of time. The molar number increases to 1.9 fmol ($1.9 \times 10^{-15} \text{ mol}$) during the 6-ms pulse, and changes only slowly afterwards due to diffusive leakage in/out of the cell. In contrast, if we artificially remove electrophoresis from Eqs. (7–12), such that only diffusion is driving molecular transport (Fig. 7a, dashed), the resulting value is much lower at 0.1 fmol. This calculation demonstrates that for this particular case, electrophoresis, and not diffusion, is the dominant mode of transport. A further study on the contribution of diffusion is found in Section 4.2, where the effect of post-pulsation PAD is examined, and the results are discussed in relation to the experimental observation by Pucihar et al. [60]. Finally, molecular delivery can be further enhanced by using an extended pulse. The dot-dashed curve in Fig. 7a shows the evolution of $[\text{Ca}^{2+}]_{\text{tot}}$ under a continuous, 150-ms pulse ($E_0 = 1 \text{ kV/cm}$). The final value reaches 22.4 fmol, which is another order of magnitude higher than that with a 6-ms pulse. For this case, the bulk of Ca^{2+} continues to spread within the cell until reaching the opposite side (Fig. 7b), filling the entire cell at a concentration of approximately 10.5 mM (see Movie 3 in the online supplementary material). At this point, a steady-state is reached, as the influx and efflux from respectively the anode- and cathode-facing caps equate. Note that such a long pulse and high Ca^{2+} concentration will likely irreversibly damage the cell. However, here we are simply theoretically delineating the upper limit of electrophoretically-mediated molecular delivery using Ca^{2+} as a generic example.

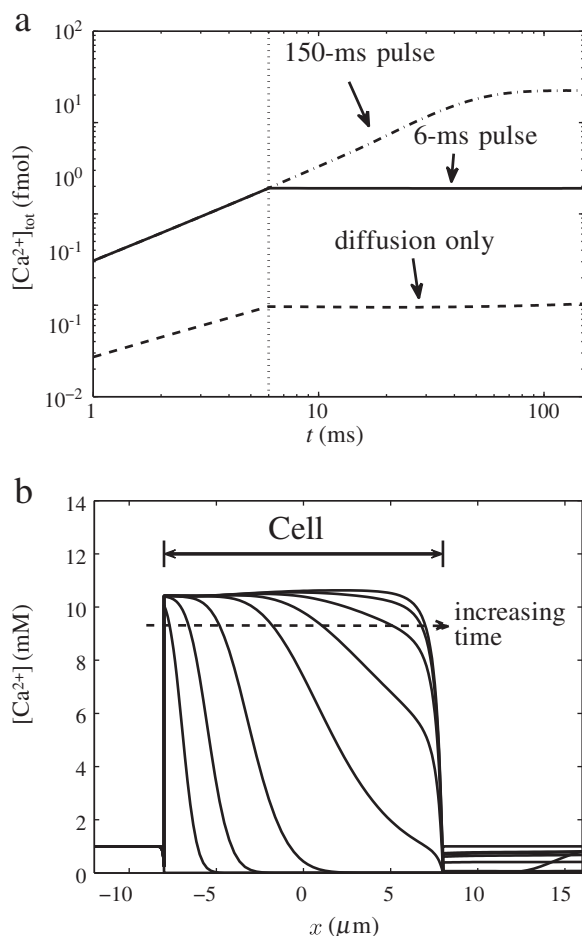


Fig. 7. a) Total Ca^{2+} within the cell ($[\text{Ca}^{2+}]_{\text{tot}}$) with different mechanisms. b) Ca^{2+} concentration along the cell centerline with a 150-ms-long pulse at 1 kV/cm. The times correspond to $t = 0, 1.1 \text{ ms}, 3.3 \text{ ms}, 10 \text{ ms}, 30 \text{ ms}, 50 \text{ ms}, 70 \text{ ms}, 90 \text{ ms},$ and 120 ms .

4. Discussions

4.1. The effect of the membrane permeabilization on FASS

In the previous section, we presented results on simulated ionic transport in, across, and around an electroporated cell. Although our emphasis has been on the species concentrations, the results do depend on the permeabilization calculation via the ASE model. In what follows, such dependence is discussed.

When deriving the relation (15), we presented an idealized argument by ignoring diffusion and assuming $c_e = c_{e,o}$, and we have not considered the presence of the membrane. The latter, however, can have complex effects on the detailed transport dynamics. Fig. 8a shows an up-close view of Ca^{2+} concentration around the anode-facing membrane ($x = -8 \mu\text{m}$) at the end of a 6-ms pulse, and again we focus our study along the cell centerline. A clear depletion is shown outside the cell. This is because if the initial extracellular concentration, $[\text{Ca}^{2+}]_{e,o}$, is used to calculate F_m and F_e , the condition $F_m > F_e$ will result which violates the flux continuity (Eq. (10)). Therefore, the extracellular concentration near the membrane has to adjust (decrease) to lower F_m . Meanwhile, although the electrophoretic component in F_e decreases along with $[\text{Ca}^{2+}]_e$, the diffusive component increases as the concentration gradient becomes favorable, resulting in a final balance between F_m and F_e .

Conversely, if using $[\text{Ca}^{2+}]_{e,o}$ in evaluating F_m and F_e results in the condition $F_m < F_e$, then ion accumulation outside the membrane occurs, as shown in Fig. 8b. For these cases, we artificially reduce ρ_p by 10

(denoted by $0.1\rho_p$) and 100 (denoted by $0.01\rho_p$) times, respectively, to demonstrate this effect. That is, we multiply the ρ_p variable calculated from the ASE model by 0.1 and 0.01, respectively, while keeping all other parameters un-changed. In such situations, the decrease in ρ_p requires an increase in $[\text{Ca}^{2+}]_e$ (accumulation) to balance the fluxes. These two effects in part compensate each other in determining the final F_m . The extracellular diffusive fluxes for both cases are opposite to the electrophoretic fluxes. The Γ values from the simulation are 10.7 for the case of $0.1\rho_p$, and 14.2 for the case of $0.01\rho_p$, respectively. Most interestingly, these values are higher when compared to the original case shown in Fig. 8a, for which $\Gamma = 10.5$ from the simulation. (For all cases, the theory predicts $\Gamma = 10.5$ from Eq. (15).) This behavior is counter-intuitive, as the membrane is actually less permeabilized. An explanation is found in Appendix C, where we show that the two-dimensional effect which we have not considered so far also has important contributions.

The above results indicate that molecular transport into an electroporated cell involves complex dynamic processes. On the other hand, they also demonstrate that FASS is a robust mechanism which does not strongly depend on the specific state of the membrane. That is, we have varied the degree of membrane permeabilization by two-orders of magnitude, and observed similar stacking behavior in the intracellular concentration, although some quantitative variations exist in the final Γ values. In a sense, the depletion/accumulation effects are means to modulate the membrane fluxes toward a stable equilibrium value.

In our simulations, the predicted maximum ρ_p value corresponds to a membrane area loss of around 0.8% during the presence of the electric field. This value is high when compared with those from the literature, e.g., 0.01–0.1% as estimated by Kinosita et al. [16]. The cases studied in Fig. 8b bring the ρ_p values to exactly this range. We therefore argue that FASS should be observed across a membrane with a realistic degree of permeabilization. On the other hand, the discrepancy in ρ_p between the simulation and the experiment is possibly due to the difference in the parametric configuration in the current study and that used by Kinosita et al. [16]. Using $\sigma_e = 5 \text{ S/m}$, $\sigma_i = 0.455 \text{ S/m}$, $a = 50 \mu\text{m}$, and $E_0 = 100 \text{ V/cm}$ [16,38], the ASE model yields a ρ_p value of 0.2%, which is in much closer agreement with the experimental data. The details are not shown for brevity.

4.2. The effect of free diffusion post-pulsation

In Fig. 7, we have shown that diffusion plays a secondary role in transport, and the delivered molecules through this mechanism is an order of magnitude less than those by electrophoresis during a 6-ms pulse. More importantly, once the pulse ceases, the total molar content within the cell remains approximately constant, and no significant exchange across the membrane occurs (Fig. 7, solid line). This is simply because the PAD decreases immediately (with a characteristic time of $10 \mu\text{s}$) by 3 orders of magnitude (from $\sim 10^{-2}$ to $\sim 10^{-5}$) post-pulsation, which results from the ASE model's capability to predict resealing. However, this result seems to contradict those by Pucihar et al. [60]. In the latter experiment, the intensity of PI within electroporated cells was tracked using a photomultiplier tube both during and after pulsation. The results indicated that PI continued to enter the cell by diffusion after the pulse ceased, and PI signal enhancement was stronger during this second stage when compared with that during the pulsation.

We hypothesize that the discrepancy between these studies might be caused by an underestimate of the PAD during resealing in the simulation. To test this hypothesis, we increase ρ_p by 10 (denoted by $10\rho_p$, dashed, Fig. 9) and 100 (denoted by $100\rho_p$, dot-dashed, Fig. 9) times for $t > 6 \text{ ms}$, respectively, while keeping all other parameters unchanged. This manipulation brings the membrane area loss from around 10^{-5} to 0.01%–0.1%, which falls within the estimated range by Kinosita et al. [16]. The resulted evolution of $[\text{Ca}^{2+}]_{\text{tot}}$ is shown in Fig. 9. For reference, the original case without a manipulation in ρ_p is also shown (denoted by “ ρ_p ”, solid). We observe that for the case of $10\rho_p$,

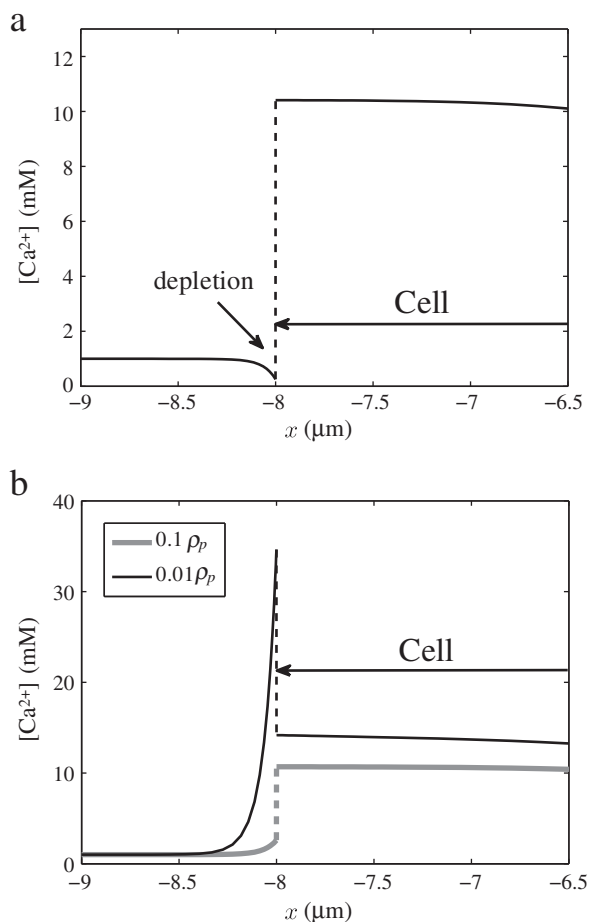


Fig. 8. a) Concentration depletion outside the cell at the end of a 6-ms pulse. The data is taken from the simulation shown in Figs. 2–5. b) Concentration accumulation outside the cell due to decreased ρ_p -values (denoted by $0.1\rho_p$ and $0.01\rho_p$, respectively). For all cases, the dashed line denotes a jump in value across the membrane.

the total molar content decreases slowly, indicating a slight leakage of Ca^{2+} from the cell to the extracellular space. For the case of $100\rho_p$, a decrease is followed by an increase at a later time. The initial decrease is mainly mediated by a leakage outward on the anode-facing cap, because $[\text{Ca}^{2+}]_i > [\text{Ca}^{2+}]_e$, whereas the eventual increase is mediated

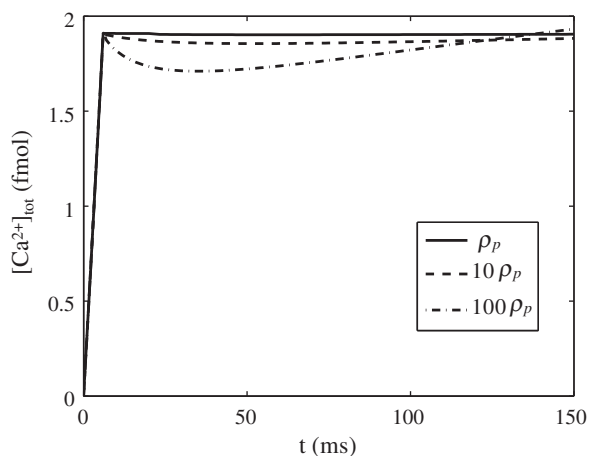


Fig. 9. The effect of post-pulsation PAD on total molar content within the cell. For the cases of $10\rho_p$ and $100\rho_p$, the PAD is increased by 10 and 100 times, respectively.

by a leakage inward on the opposite side, where $[\text{Ca}^{2+}]_e > [\text{Ca}^{2+}]_i$ (see Fig. 4a). However, neither case corroborates well with the qualitative trend observed by Pucihar et al. [60]. We speculate that the difference might be caused again by the different configurations used, i.e., by the differences in pulse length, dye molecule (PI vs. Ca^{2+}), among others. A simulation with a configuration better approximating the experimental conditions in this case may help reconcile the discrepancy, and is the scope of future work.

4.3. Experimental evidences to support FASS

In the previous section, we have demonstrated that our model prediction satisfyingly reproduced the trends observed in the fluorescence measurements in GT99. However, the data collected in the latter is insufficient to support FASS, because the preloaded Fluo-3 concentration was at a low level of 2.2 μM , whereas our predicted Ca^{2+} concentration is on the order of 10 mM. Such an experiment therefore cannot detect any enhancement beyond the limiting dye concentration. However, other experimental evidences do exist in the literature to strongly support our prediction. In Eq. (16), the theory predicts that the maximum intracellular concentration for a generic ionic species, $c_{i,\text{max}}$, is reciprocally proportional to the extracellular conductivity, σ_e . This correlation has been observed by Djuzenova et al. [76]. In this experiment, PI was delivered into murine myeloma cells, with the buffer conductivity ranging from 1 to 5 ms/cm. The PI molar content within the cells, c_{PI} , was estimated from fluorescence signals, and its correlation with σ_e was well-fitted by a reciprocal curve, $c_{PI} \propto 1/\sigma_e$. Although $c_{i,\text{max}}$ (maximum concentration) and c_{PI} (total molar number) are not exactly the same variable, the experimental data does corroborate with our theory. In a latter work by the same group [77], an inverse correlation between PI uptake and medium conductivity was again observed for nano-second pulsations, although the fitted curve was not exactly reciprocal.

Interestingly, the FASS mechanism also explains why efflux was not observed in GT99. In this work, the same authors also investigated the situation where the initial intracellular Ca^{2+} concentration ($[\text{Ca}^{2+}]_{i,0} = 220$ nM) was higher than that in the buffer ($[\text{Ca}^{2+}]_{e,0} = 100$ nM). For this case, the buffer was loaded with Fluo-3 at 10 μM to detect any elevation in the extracellular Ca^{2+} concentration, whereas the cytoplasm had no Fluo-3 initially. Intuitively, Ca^{2+} should be pushed electrophoretically out of the cathode-facing cap, such that efflux is observed. However, the experiment showed only enhanced fluorescence outside the cell on the anode- (positive-electrode-) facing side. This result nonetheless can be explained with the current model. The enhancement outside the anode-facing cap could be interpreted as accumulation similar to those shown in Fig. 8b. The extracellular region next to the cathode-facing cap, on the other hand, was possibly depleted by means of FASS. In fact, a simulation predicts that Ca^{2+} concentration in this region should be approximately 21 nM, much lower than the background value of 100 nM (not shown). Certainly, this region would be refilled by diffusion once the pulse ceases.

5. Conclusion

In this work, we have presented a numerical simulation to explore the spatio-temporal dynamics of Ca^{2+} -delivery via electroporation. The main conclusions are:

- Electrophoresis can play an important role in molecular delivery via electroporation; it provides a faster and more efficient means of transport when compared with free diffusion.
- FASS, which mechanism arises from a gradient in the electrophoretic velocity, determines the achievable molecular concentration within the cell. The latter is reciprocally correlated with the extracellular electrical conductivity.

In addition, we have also discovered that a uniform dye concentration may give rise to a non-uniform fluorescent signal, due to the three-dimensional cell geometry combined with a finite focal

depth comparable to the cell size. This result suggests that careful deconvolution and calibration need to be performed in order to extract molar concentration values from fluorescence data. Finally, the current model framework is suitable to study the transport of small molecules including free ions, drug molecules, and molecular dyes. The interaction of large molecules (such as DNA) with the membrane is much more complex, and a more sophisticated model is needed to describe these processes.

Supplementary materials related to this article can be found online at [doi:10.1016/j.bioelechem.2011.04.006](https://doi.org/10.1016/j.bioelechem.2011.04.006).

Acknowledgements

The authors acknowledge funding support from an NSF Award CBET-0747886 with Dr. William Schultz and Dr. Henning Winter as contract monitors.

Appendix A. A brief derivation of Eq. (12)

Here we present a brief derivation of the expression for the membrane flux density, F_m (Eq. (12)). Our basic assumption is that the transport of ionic species across the membrane is one-dimensional and quasi-steady. The one-dimensionality is a good approximation validated by us in an earlier work [78]. The quasi-steadiness is from a simple argument that an equilibrium is reached on a short time-scale (\sim ns) due to the small thickness of the membrane (which is assumed to be equal to the pore length). The governing equation reads

$$0 = \frac{\partial}{\partial r} \left(wFzc \frac{\partial \Phi}{\partial r} + D \frac{\partial c}{\partial r} \right), \quad (\text{A.1})$$

where c is a generic species concentration, and r is the direction along the pore-centerline, pointing from the intra- to the extra-cellular space. Integrating Eq. (A.1) once yields

$$J = - \left(wFzc \frac{\partial \Phi}{\partial r} + D \frac{\partial c}{\partial r} \right), \quad (\text{A.2})$$

where J is the total electrophoretic and diffusive flux.

The electric potential within the pore, Φ , is given by [78]:

$$\Phi(r) = \Phi_i + \frac{V_m}{\ln \gamma} \ln(\sigma(r) / \sigma_i), \quad (\text{A.3})$$

where Φ_i is the intracellular potential at the pore interface, $\gamma = \sigma_e / \sigma_i$ is the conductivity ratio, and $\sigma(r) = \sigma_i + (\sigma_e - \sigma_i)r/h$ is the conductivity distribution function within the pore. Eq. (A.3) is derived by solving an one-dimensional Ohmic equation using this conductivity profile. Eq. (A.2) can be further integrated using c_i and c_e (the intra- and extra-cellular molar concentrations) as boundary conditions on the two ends of the pore. The flux J is determined as an integration constant:

$$J = \frac{D(Pe - \ln \gamma)}{h} \frac{(\gamma - 1)}{\ln \gamma} \frac{(c_e - c_i \exp(Pe))}{(\gamma - \exp(Pe))}, \quad (\text{A.4})$$

where $Pe \equiv -wFzV_m/D$ is a Péclet number. For $\gamma = 1$ (no conductivity gradient), Eq. (A.4) is reduced to

$$J = \frac{PeD}{h} \frac{c_e - c_i \exp(Pe)}{1 - \exp(Pe)}. \quad (\text{A.5})$$

The exponential dependence of the flux on Pe warrants further discussion. In the limit of large Péclet numbers, Eq. (A.4) becomes

$$J = \begin{cases} -\frac{wFzV_m}{h} \frac{\gamma - 1}{\gamma \ln \gamma} c_e, & \text{for } V_m > 0, \\ -\frac{wFzV_m}{h} \frac{\gamma - 1}{\ln \gamma} c_i, & \text{for } V_m < 0. \end{cases} \quad (\text{A.6})$$

We realize that Eq. (A.6) is simply an upwind scheme. That is, for large values of V_m , the flux is solely determined by the concentration on the high-potential side (c_e for $V_m > 0$, and c_i for $V_m < 0$, where $V_m \equiv \Phi_e - \Phi_i$). This result is a natural consequence from the fact that for large Pe , electrophoresis dominates diffusion. For our system and for $V_m = 0.5$ V, $Pe \sim 40$. In this case, Eq. (A.6) is a very good approximation to Eq. (A.4). However, we use Eq. (A.4) for completeness.

Finally, the expression for F_m is obtained by simply weighting Eq. (A.4) with the PAD, ρ_p . Effectively, we assume that Ca^{2+} and other pertinent ions can pass through all pores without any energy barrier. This assumption may require revision when larger molecules are considered, where the size-exclusion and other effects may become important.

Appendix B. The effect of electroosmotic flow on molecular transport

Under physiological conditions, the surfaces of the cell membrane are usually negative charged [86,87]. These charged surfaces induce an electroosmotic flow around the membrane when an electric field is applied. In the context of species transport, such flow leads to a convective effect in addition to electrophoresis, which may modify the results from the NP framework (Eqs. (7–12)) where it is not included. Here we briefly estimate its importance and the impact on our main conclusions.

For a charged surface with a zeta potential, ζ , the velocity of the induced electroosmotic flow is given by

$$U_{eo} = -\frac{\varepsilon \zeta E_t}{\mu},$$

where ε and μ are respectively the permittivity and the viscosity of the buffer solution, and E_t is the tangential field. An estimate of its relative importance to electrophoresis can be given by evaluating the ratio of the two velocities,

$$\frac{U_{eo}}{U_{ep}} = -\frac{\varepsilon \zeta}{\mu wFz}.$$

From the literature [87], the zeta potential of a mammalian cell is on the order of -20 to -30 mV. Provided that this value range applies to CHO cells, the resulting ratio is around $0.2 \sim 0.3$ using typical values ($\varepsilon = 6.9 \times 10^{-10}$ F/m, $\mu = 1 \times 10^{-3}$ kg/m \cdot s, $\omega_{\text{Ca}^{2+}} = 3.2 \times 10^{-13}$ mol \cdot s/kg, and $z = +2$). The effect of convective electroosmotic transport is therefore appreciable yet not significant when compared with the main mechanism, namely, electrophoretic transport. Note that a strong applied electric field such as that used in electroporation does not appreciably modify the zeta potential. The modification is on the order of $E_0 \lambda_D$, where λ_D is the Debye length [88]. For typical E_0 (~ 1 kV/cm) and λ_D (~ 1 nm) values relevant to our study, the induced change in the zeta potential is less than 1% and negligible.

While the above estimate applies to an intact membrane, the situation for an electroosmotic flow within an electropore could be more complex. The zeta-potential may differ from that of the integrated membrane, and in addition an electrohydrodynamic flow can be induced due to charge accumulation within the pore (see an earlier work by us, [78]). However, here in the absence of experimental data

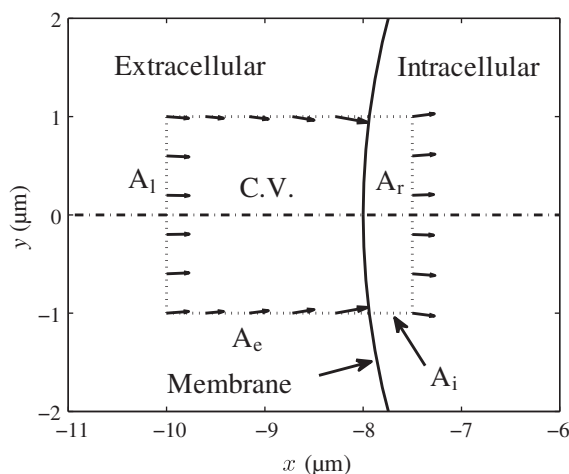


Fig. C.10. A two-dimensional control volume (C.V.) analysis of the transport effects. The area element A_l is away from the membrane such that the concentration is ambient ($c_{e,o}$). The element A_r is close to the membrane such that the flux through A_l is negligible. The arrows denote the direction of the local electric field.

(e.g., zeta potential measurements for electropores) to support a realistic estimate, we assume the effect is on the same order as for the intact membrane, and hence neglect it by approximation.

Most importantly, our results are robust with respect to variations in flux calculation (Eqs. (11, 12)). As we have demonstrated in Section 4.1, a modification on net flux density across the pores, F_m , will be automatically rectified by an accumulation or depletion of the ions outside of the cell. Two order of variation in flux calculation (see Fig. 8, where the variation is due to adjustments in the pore area density) does not lead to significant modifications of the resulting intracellular concentration profile, and the final flux across the membrane is largely determined by the extracellular flux density, F_e . We therefore argue that even in the case that electroosmotic flow within the pore does significantly contribute to the membrane flux, the final results on species concentration do not change appreciably, and FASS still provides a dominant mechanism for ionic transport.

Appendix C. The two-dimensional effects in electrophoretic molecular transport

In the previous sections, we have presented a simplified, one-dimensional argument to explain the FASS mechanism. Although the resulting formula predicts the stacking behavior with reasonable accuracy, it does not explain the anti-intuitive behavior that a decrease in ρ_p leads to an increase in Γ (Fig. 8). Here we demonstrate that this behavior results from the two-dimensional effect which we have so far not considered in the argument.

Fig. C.10 shows a control volume across the membrane at the cell center plane. The area element A_l is far enough from the membrane, such that the concentration is ambient ($c_{e,o}$). The area element A_r is within the cell and very close to the membrane, so that the flux from the side area element, A_i , is negligible. Note that due to the axisymmetry (with respect to the dot-dashed line), the control volume is in fact a cylinder, with A_r and A_l being the end-disks, and A_e , the side envelope. The directions of the electric field on the boundaries are shown as vectors. On A_e , they point inward, due to the conducting pathway offered by the permeabilized membrane caps. At steady-state, the continuity of flux requires that $F_r + F_l + F_e = 0$, where the three terms are respectively the flux on A_r , A_l , and A_e . For Fig. 8a, the depletion effect results in a very small molar concentration on A_e , and hence $F_e \ll F_r, F_l$. (Note that F is linearly proportional to c .) This simplification reduces the analysis back to be one-dimensional, and explains why Eq. (15) provides an excellent agreement when compared with the Γ -value from

simulation for this case. On the other hand, when accumulation (Fig. 8b) occurs, c_e on the area element A_e is much greater than $c_{e,o}$, and F_e has a non-negligible contribution to the flux balance. Due to the inward direction of the electric field vectors, this contribution increases F_r , hence leading to higher $c_{i,max}$ and Γ values. Note that in the above argument, we again temporarily ignored the diffusive fluxes for simplicity.

References

- [1] E. Neumann, M. Schaefer-Ridder, Y. Wang, P.H. Hofschneider, Gene transfer into electric fields mouse lymphoma cells by electroporation in high electric field, *EMBO J.* 7 (1982) 841–845.
- [2] E. Neumann, A.E. Sowers, C.A. Jordan (Eds.), *Electroporation and Electrofusion in Cell Biology*, Plenum Press, 1989.
- [3] M. Bettan, M.A. Ivanov, L.M. Mir, F. Boissiere, P. Delaere, D. Scherman, Efficient DNA electrotransfer into tumors, *Bioelectrochemistry* 52 (2000) 83–90.
- [4] M. Golzio, J. Teissié, M. Rols, Control by membrane order of voltage-induced permeabilization, loading and gene transfer in mammalian cells, *Bioelectrochemistry* 53 (2000) 25–34.
- [5] L.M. Mir, Therapeutic perspectives of *in vivo* cell electroporation, *Bioelectrochemistry* 53 (2000) 1–10.
- [6] G.T. Martin, U.F. Pliquet, J.C. Weaver, Theoretical analysis of localized heating in human skin subjected to high voltage pulses, *Bioelectrochemistry* 57 (2002) 55–64.
- [7] J. Gehl, Electroporation: theory and methods, perspectives for drug delivery, gene therapy and research, *Acta Physiol. Scand.* 177 (2003) 437–447.
- [8] U. Pliquet, R. Elez, A. Piiper, E. Neumann, Electroporation of subcutaneous mouse tumors by rectangular and trapezium high voltage pulses, *Bioelectrochemistry* 62 (2004) 83–93.
- [9] U. Pliquet, S.G. T. S. Huib, C. Gusbetha, E. Neumann, Local and transient structural changes in stratum corneum at high electric fields: contribution of joule heating, *Bioelectrochemistry* 67 (2005) 37–46.
- [10] J. Teissié, M. Golzio, M.P. Rols, Mechanisms of cell membrane electroporation: a minireview of our present (lack of ?) knowledge, *Biochim. Biophys. Acta* 1724 (2005) 270–280.
- [11] J.M. Escoffre, T. Portet, L. Wasungu, J. Teissié, D. Dean, M.P. Rols, What is (still not) known of the mechanism by which electroporation mediates gene transfer and expression in cells and tissues, *Mol. Biotechnol.* 41 (2009) 286–295.
- [12] A.O. Bilka, K.A. DeBruin, W. Krassowska, Theoretical modeling of the effects of shock duration, frequency, and strength on the degree of electroporation, *Bioelectrochemistry* 51 (2000) 133–143.
- [13] C. Barrau, J. Teissié, B. Gabriel, Osmotically induced membrane tension facilitates the triggering of living cell electroporation, *Bioelectrochemistry* 63 (2004) 327–332.
- [14] S. Talele, P. Gaynor, Non-linear time domain model of electroporation: response of a single cell to an arbitrary applied electric field, *J. Electrostat.* 65 (2007) 775–784.
- [15] D. Gross, L.M. Loew, W.W. Webb, Optical imaging of cell membrane potential changes induced by applied electric fields, *Biophys. J.* 50 (1986) 339–348.
- [16] K. Kinoshita, I. Ashikawa, N. Saita, H. Yoshimura, H. Itoh, K. Nagayama, A. Ikegami, Electroporation of cell membrane visualized under a pulsed-laser fluorescence microscope, *Biophys. J.* 53 (1988) 1015–1019.
- [17] M. Hibino, M. Shigemori, H. Itoh, K. Nagayama, K. Kinoshita, Membrane conductance of an electroporated cell analyzed by submicrosecond imaging of transmembrane potential, *Biophys. J.* 59 (1991) 209–220.
- [18] W. Frey, J.A. White, R.O. Price, P.F. Blackmore, R.P. Joshi, R. Nuccitelli, S.J. Beebe, K.H. Schoenbach, J.F. Kolb, Plasma membrane voltage changes during nanosecond pulsed electric field exposure, *Biophys. J.* 90 (2006) 3608–3615.
- [19] J.C. Weaver, Y.A. Chizmadzhev, Theory of electroporation: a review, *Bioelectrochem. Bioenerg.* 41 (1996) 135–160.
- [20] P. Kramar, D. Miklavcic, A.M. Lebar, Determination of the lipid bilayer breakdown voltage by means of linear rising signal, *Bioelectrochemistry* 70 (2007) 23–27.
- [21] D.C. Chang, T.S. Reese, Changes in membrane structure induced by electroporation as revealed by rapid-freezing electron microscopy, *Biophys. J.* 58 (1990) 1–12.
- [22] H. Leontiadou, A.E. Mark, S.J. Marrink, Molecular dynamics simulations of hydrophilic pores in lipid bilayers, *Biophys. J.* 86 (2004) 2156–2164.
- [23] D.P. Tieleman, The molecular basis of electroporation, *BMC Biochem.* 5 (2004) 10.
- [24] A.A. Gurtovenko, I. Vattulainen, Pore formation coupled to ion transport through lipid membranes as induced by transmembrane ionic charge imbalance: atomistic molecular dynamics study, *J. Am. Chem. Soc.* 127 (2005) 17570–17571.
- [25] M. Tarek, Membrane electroporation: a molecular dynamics simulation, *Biophys. J.* 88 (2005) 4045–4053.
- [26] J. Wohler, W.K. den Otter, O. Edholm, W.J. Briels, Free energy of a trans-membrane pore calculated from atomistic molecular dynamics simulations, *J. Chem. Phys.* 124 (2006) 154905.
- [27] U. Pliquet, R.P. Joshi, V. Sridhara, K.H. Schoenbach, High electrical field effects on cell membranes, *Bioelectrochemistry* 70 (2007) 275–282.
- [28] M.L. Fernández, G. Marshall, F. Sagués, R. Reigada, Structural and kinetic molecular dynamics study of electroporation in cholesterol-containing bilayers, *J. Phys. Chem. B* 114 (20) (2010) 6855–6865.
- [29] Z.A. Levine, P.T. Vernier, Life cycle of an electropore: field-dependent and field-independent steps in pore creation and annihilation, *J. Membr. Biol.* 236 (2010) 27–36.

- [30] A. Barnett, J.C. Weaver, Electroporation: a unified, quantitative theory of reversible electrical breakdown and rupture in artificial planar bilayer membranes, *Bioelectrochem. Bioenerg.* 25 (1991) 163–182.
- [31] S.A. Freeman, M.A. Wang, J.C. Weaver, Theory of electroporation of planar bilayer membranes: prediction of the aqueous area, change in capacitance, and pore-pore separation, *Biophys. J.* 67 (1994) 42–56.
- [32] V.F. Pastushenko, Y.A. Chizmadzhev, V.B. Arakelyan, Electric breakdown of bilayer lipid membranes II: Calculation of the membrane lifetime in the steady-state diffusion approximation, *Bioelectrochem. Bioenerg.* 6 (1979) 53–62.
- [33] Z. Vasilkoski, A.T. Esser, T.R. Gowrishankar, J.C. Weaver, Membrane electroporation: the absolute rate equation and nanosecond time scale pore creation, *Phys. Rev. E* 74 (2006) 021904.
- [34] J.C. Neu, W. Krassowska, Asymptotic model of electroporation, *Phys. Rev. E* 59 (3) (1999) 3471–3482.
- [35] J.C. Neu, W. Krassowska, Modeling postshock evolution of large electropores, *Phys. Rev. E* 67 (2003) 021915.
- [36] K.A. DeBruin, W. Krassowska, Modeling electroporation in a single cell. I. Effects of field strength and rest potential, *Biophys. J.* 77 (1999) 1213–1224.
- [37] K.A. DeBruin, W. Krassowska, Modeling electroporation in a single cell. II. Effects of ionic concentrations, *Biophys. J.* 77 (1999) 1225–1233.
- [38] W. Krassowska, P.D. Filev, Modeling electroporation in a single cell, *Biophys. J.* 92 (2007) 404–417.
- [39] D.A. Stewart, T.R. Gowrishankar, J.C. Weaver, Transport lattice approach to describing cell electroporation: use of a local asymptotic model, *IEEE Trans. Plasma Sci.* 32 (4) (2004) 1696–1708.
- [40] A.T. Esser, K.C. Smith, T.R. Gowrishankar, J.C. Weaver, Towards solid tumor treatment by irreversible electroporation: intrinsic redistribution of fields and currents in tissue, *Technol. Cancer Res. Treat.* 6 (2007) 261.
- [41] K.C. Smith, T.R. Gowrishankar, A.T. Esser, D.A. Stewart, J.C. Weaver, The spatially distributed dynamic transmembrane voltage of cells and organelles due to 10-ns pulses: meshed transport networks, *IEEE Trans. Plasma Sci.* 34 (4) (2006) 1394–1404.
- [42] K.C. Smith, J.C. Weaver, Active mechanisms are needed to describe cell responses to submicrosecond, megavolt-per-meter pulses: cell models for ultrashort pulses, *Biophys. J.* 95 (2008) 1547–1563.
- [43] T.R. Gowrishankar, J.C. Weaver, Electrical behavior and pore accumulation in a multicellular model for conventional and supra-electroporation, *Biochem. Biophys. Res. Comm.* 349 (2006) 643–653.
- [44] T.R. Gowrishankar, A.T. Esser, Z. Vasilkoski, K.C. Smith, J.C. Weaver, Microdosimetry for conventional and supra-electroporation in cells with organelles, *Biochem. Biophys. Res. Commun.* 341 (2006) 1266–1276.
- [45] T.R. Gowrishankar, D.A. Stewart, J.C. Weaver, Model of a confined spherical cell in uniform and heterogeneous applied electric fields, *Bioelectrochemistry* 68 (2006) 181–190.
- [46] R.P. Joshi, K.H. Schoenbach, Electroporation dynamics in biological cells subjected to ultrafast electrical pulses: a numerical simulation study, *Phys. Rev. E* 62 (1) (2000) 1025–1033.
- [47] R.P. Joshi, Q. Hu, R. Aly, K.H. Schoenbach, Self-consistent simulations of electroporation dynamics in biological cells subjected to ultrashort electrical pulses, *Phys. Rev. E* 64 (2001) 011913.
- [48] R.P. Joshi, Q. Hu, K.H. Schoenbach, S.J. Beebe, Simulations of electroporation dynamics and shape deformations in biological cells subjected to high voltage pulses, *IEEE Trans. Plasma Sci.* 30 (4) (2002) 1536–1546.
- [49] R.P. Joshi, Q. Hu, K.H. Schoenbach, Dynamical modeling of cellular response to short-duration, high-intensity electric fields, *IEEE Trans. Dielectr. Electr. Insul.* 10 (5) (2003) 778–787.
- [50] M. Rols, J. Teissié, Electroporation of mammalian cells to macromolecules: control by pulse duration, *Biophys. J.* 75 (1998) 1415–1423.
- [51] V.A. Klenchin, S.I. Sukharev, S.M. Serov, L.V. Chernomordik, Y.A. Chizmadzhev, Electrically induced DNA uptake by cells is a fast process involving DNA electroporation, *Biophys. J.* 60 (1991) 804–811.
- [52] H. Wolf, M.P. Rols, E. Boldt, E. Neumann, J. Teissié, Control by pulse parameters of electric field-mediated gene transfer in mammalian cells, *Biophys. J.* 66 (1994) 524–531.
- [53] M.F. Bureau, J. Gehl, V. Deleuze, L.M. Mir, D. Scherman, Importance of association between permeabilization and electrophoretic forces for intramuscular DNA electrotransfer, *Biochim. Biophys. Acta* 1474 (2000) 353–359.
- [54] S.I. Sukharev, V.A. Klenchin, S.M. Serov, L.V. Chernomordik, Y.A. Chizmadzhev, Electroporation and electrophoretic DNA transfer into cells, *Biophys. J.* 63 (1992) 1320–1327.
- [55] K.J. Müller, M. Horbaschek, K. Lucas, U. Zimmermann, V.L. Sukhorukov, Electrotransfection of anchorage-dependent mammalian cells, *Exp. Cell Res.* 288 (2003) 344–353.
- [56] D.A. Zaharoff, J.W. Henshaw, B. Mossop, F. Yuan, Mechanistic analysis of electroporation-induced cellular uptake of macromolecules, *Exp. Biol. Med.* 233 (1) (2008) 94–105.
- [57] J. Teissié, J.M. Escoffre, M.P. Rols, M. Golzio, Time dependence of electric field effects on cell membranes. A review for a critical selection of pulse duration for therapeutic applications, *Radiol. Oncol.* 42 (4) (2008) 196–206.
- [58] M. Golzio, J. Teissié, M. Rols, Direct visualization at the single-cell level of electrically mediated gene delivery, *Proc. Nat. Acad. Sci. U. S. A.* 99 (3) (2002) 1292–1297.
- [59] M.S. Venslauskas, S. Šatkauskas, R. Rodaitė-Riševičienė, Efficiency of the delivery of small charged molecules into cells in vitro, *Bioelectrochemistry* 79 (2010) 130–135.
- [60] G. Pucihar, T. Kotnik, D. Miklavčič, J. Teissié, Kinetics of transmembrane transport of small molecules into electroporated cells, *Biophys. J.* 95 (2008) 2837–2848.
- [61] A. Denet, R. Vanbever, V. Prêat, Skin electroporation for transdermal and topical delivery, *Adv. Drug Delivery Rev.* 56 (2004) 659–674.
- [62] M.R. Prausnitz, V.G. Bose, R. Langer, J.C. Weaver, Electroporation of mammalian skin: a mechanism to enhance transdermal drug delivery, *Proc. Natl. Acad. Sci.* 90 (1993) 10504–10508.
- [63] R. Vanbever, N. Lecouturier, V. Prêat, Transdermal delivery of metoprolol by electroporation, *Pharm. Res.* 11 (11) (1994) 1657–1662.
- [64] R. Vanbever, E.L. Boulengé, V. Prêat, Transdermal delivery of fentanyl by electroporation I. Influence of electrical factors, *Pharm. Res.* 13 (4) (1996) 559–565.
- [65] V. Regnier, N.D. Morre, A. Jadoul, V. Prêat, Mechanisms of a phosphorothioate oligonucleotide delivery by skin electroporation, *Int. J. Pharm.* 184 (1999) 147–156.
- [66] V. Prêat, R. Vanbever, Skin electroporation for transdermal and topical drug delivery, in: R.H. Guy, J. Hadgraft (Eds.), *Transdermal Drug Delivery*, 2nd Edition, Marcel Dekker, Vol. 123, 2002, pp. 227–254.
- [67] K.C. Smith, J.C. Neu, W. Krassowska, Model of creation and evolution of stable electropores for DNA delivery, *Biophys. J.* 86 (2004) 2813–2826.
- [68] M. Puc, T. Kotnik, L.M. Mir, D. Miklavčič, Quantitative model of small molecules uptake after *in vitro* cell electroporation, *Bioelectrochemistry* 60 (2003) 1–10.
- [69] Z. Rong, Bipartite expressions for diffusional mass transport in biomembranes, *Biophys. J.* 91 (2006) 4690–4696.
- [70] R. Shirakashi, V.L. Sukhorukov, I. Tanasawa, U. Zimmermann, Measurement of the permeability and resealing time constant of the electroporated mammalian cell membranes, *Int. J. Heat Mass Transf.* 47 (2004) 4517–4524.
- [71] D. Miklavčič, L. Towhid, Numerical study of the electroporation pulse shape effect on molecular uptake of biological cells, *Radiol. Oncol.* 44 (2010) 34–41.
- [72] Y. Granot, B. Rubinsky, Mass transfer model for drug delivery in tissue cells with reversible electroporation, *Int. J. Heat Mass Transf.* 51 (2008) 5610–5616.
- [73] B. Gabriel, J. Teissié, Time courses of mammalian cell electroporation observed by millisecond imaging of membrane property changes during the pulse, *Biophys. J.* 76 (1999) 2158–2165.
- [74] R. Chien, D.S. Burgi, Field amplified sample injection in high-performance capillary electrophoresis, *J. Chromatogr.* 559 (1991) 141–152.
- [75] R. Bharadwaj, J.G. Santiago, Dynamics of field-amplified sample stacking, *J. Fluid Mech.* 543 (2005) 57–92.
- [76] C.S. Djuzenova, U. Zimmermann, H. Frank, V.L. Sukhorukov, E. Richter, G. Fuhr, Effect of medium conductivity and composition on the uptake of propidium iodide into electroporated myeloma cells, *Biochim. Biophys. Acta* 1284 (1996) 143–152.
- [77] K.J. Müller, V.L. Sukhorukov, U. Zimmermann, Reversible electroporation of mammalian cells by high-intensity, ultra-short pulses of submicrosecond duration, *J. Membr. Biol.* 184 (2001) 161–170.
- [78] J. Li, H. Lin, The current-voltage relation for electropores with conductivity gradients, *Biomicrofluidics* 4 (2010) 013206.
- [79] M. Schmeer, T. Seipp, U. Pliquet, S. Kakorin, E. Neumann, Mechanism for the conductivity changes caused by membrane electroporation of CHO cell-pellets, *Phys. Chem. Chem. Phys.* 6 (2004) 5564–5574.
- [80] E.S. Buescher, K.H. Schoenbach, Effects of submicrosecond, high intensity pulsed electric fields on living cells – intracellular electromanipulation, *IEEE Trans. Dielectr. Electr. Insul.* 10 (5) (2003) 788–794.
- [81] E. Tekle, H. Oubrahim, S.M. Dzekunov, J.F. Kolb, K.H. Schoenbach, P.B. Chock, Selective field effects on intracellular vacuoles and vesicle membranes with nanosecond electric pulses, *Biophys. J.* 89 (2005) 274–284.
- [82] J.A. White, P.F. Blackmore, K.H. Schoenbach, S.J. Beebe, Stimulation of capacitive calcium entry in HL-60 cells by nanosecond pulsed electric fields, *J. Biol. Chem.* 279 (22) (2004) 22964–22972.
- [83] B. Gabriel, J. Teissié, Fluorescence imaging in the millisecond time range of membrane electroporation of single cells using a rapid ultra-low-light intensifying detection system, *Eur. Biophys. J.* 27 (1998) 291–298.
- [84] G.D. Smith, J.E. Keizer, M.D. Stern, W.J. Lederer, H. Cheng, A simple numerical model of calcium spark formation and detection in cardiac myocytes, *Biophys. J.* 75 (1998) 15–32.
- [85] E.L. Cussler, *Diffusion. Mass Transfer in Fluid Systems*, 2nd Edition, Cambridge University Press, 1997.
- [86] B. Lindholm-Sethson, Supported lipid membranes for reconstitution of membrane proteins, in: M.D. Cuyper, J.W.M. Bulte (Eds.), *Physics and Chemistry Basis of Biotechnology*, Springer Netherlands, Vol. 7, 2002, pp. 131–165.
- [87] Y. Zhang, M. Yang, N.G. Portney, D. Cui, G. Budak, E. Ozbay, M. Ozkan, C.S. Ozkan, Zeta potential: a surface electrical characteristic to probe the interaction of nanoparticles with normal and cancer human breast epithelial cells, *Biomaterials* 10 (2008) 321–328.
- [88] F. Elinder, P. Århem, Role of individual surface charges of voltage-gated K channels, *Biophys. J.* 77 (1999) 1358–1362.
- [89] R. Hölzel, I. Lamprecht, Dielectric properties of yeast cells as determined by electrorotation, *Biochim. Biophys. Acta* 1104 (1992) 195–200.